



# Pre-acquired CT-based attenuation correction with automated headrest removal for a brain-dedicated PET system

Yuma Iwao<sup>1</sup> · Go Akamatsu<sup>1</sup> · Hideaki Tashima<sup>1</sup> · Miwako Takahashi<sup>1</sup> · Taiga Yamaya<sup>1</sup>

Received: 19 April 2023 / Revised: 21 September 2023 / Accepted: 22 September 2023 / Published online: 11 October 2023  
© The Author(s), under exclusive licence to Japanese Society of Radiological Technology and Japan Society of Medical Physics 2023

## Abstract

Attenuation correction (AC) is essential for quantitative positron emission tomography (PET) images. Attenuation coefficient maps ( $\mu$ -maps) are usually generated from computed tomography (CT) images when PET-CT combined systems are used. If CT has been performed prior to PET imaging, pre-acquired CT can be used for brain PET AC, because the human head is almost rigid. This pre-acquired CT-based AC approach is suitable for stand-alone brain-dedicated PET, such as VRAIN (ATOX Co. Ltd., Tokyo, Japan). However, the headrest of PET is different from the headrest in pre-acquired CT images, which may degrade the PET image quality. In this study, we prepared three different types of  $\mu$ -maps: (1) based on the pre-acquired CT, where namely the headrest is different from the PET system ( $\mu$ -map-*diffHr*); (2) manually removing the headrest from the pre-acquired CT ( $\mu$ -map-*noHr*); and (3) artificially replacing the headrest region with the headrest of the PET system ( $\mu$ -map-*sameHr*). Phantom images by VRAIN using each  $\mu$ -map were investigated for uniformity, noise, and quantitative accuracy. Consequently, only the uniformity of the images using  $\mu$ -map-*diffHr* was out of the acceptance criteria. We then proposed an automated method for removing the headrest from pre-acquired CT images. In comparisons of standardized uptake values in nine major brain regions from the <sup>18</sup>F-fluoro-2-deoxy-D-glucose-PET of 10 healthy volunteers, no significant differences were found between the  $\mu$ -map-*noHr* and the  $\mu$ -map-*sameHr*. In conclusion, pre-acquired CT-based AC with automated headrest removal is useful for brain-dedicated PET such as VRAIN.

**Keywords** PET · Brain · Attenuation correction · Automated headrest removing · VRAIN

## 1 Introduction

Positron emission tomography (PET) can be used to quantitatively measure in vivo biological functions at the molecular level. Attenuation correction (AC) is essential for ensuring the quantitative accuracy of PET. Figure 1 shows brain <sup>18</sup>F-fluoro-2-deoxy-D-glucose (<sup>18</sup>F-FDG) PET images with and without AC. On PET images without AC, uptake in the central brain areas was obviously lower than that with AC

due to photon attenuation. This suggests that AC should be applied to brain PET images. For stand-alone PET systems, transmission scanning with an external radiation source is a standard method to obtain the AC map ( $\mu$ -map) [1]. For PET-CT combined systems, which are more popular at present,  $\mu$ -maps can be generated from computed tomography (CT) images measured immediately prior to PET imaging, where the headrest was the same for both the PET and CT [2].

In recent years, several brain-dedicated PET systems have been developed to achieve high spatial resolution and high sensitivity while reducing the number of detectors [3, 4]. In our laboratory, we developed the first hemispherical brain-dedicated PET [5, 6], VRAIN (ATOX Co. Ltd., Tokyo, Japan), which could visualize small nuclei in healthy volunteers using <sup>18</sup>F-FDG [7]. Since VRAIN is a stand-alone PET system, it is necessary to somehow generate a  $\mu$ -map. To avoid additional radiation exposure to the patient, it is preferable to generate the  $\mu$ -map from a CT that was previously acquired for other purposes, rather than performing an

✉ Yuma Iwao  
iwao.yuma@qst.go.jp

✉ Go Akamatsu  
akamatsu.go@qst.go.jp

✉ Taiga Yamaya  
yamaya.taiga@qst.go.jp

<sup>1</sup> Department of Advanced Nuclear Medicine Sciences,  
Institute for Quantum Medical Science, National Institutes  
for Quantum Science and Technology (QST), 4-9-1  
Anagawa, Inage-Ku, Chiba 263-8555, Japan

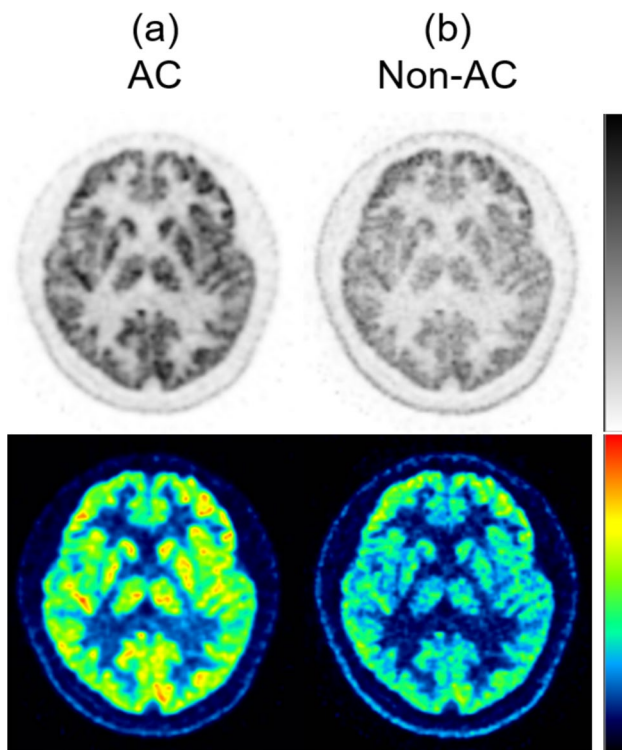


**Fig. 1** Brain  $^{18}\text{F}$ -FDG-PET images with (a) and without (b) attenuation correction

additional CT scan. In many scenarios, CT images may be obtained before PET imaging. For example, in patients with brain tumors, CT scan is performed to delineate the target volume for radiation therapy [8]. In other cases, CT images may be obtained if the patient has previously undergone whole-body or brain PET/CT imaging.

However, when using CT images acquired by another system, it is necessary to consider the differences in imaging conditions. One of the problems is the difference in patient position and angle between PET and CT images. In a previous study, an image registration method that aligns the patient position between PET and CT was reported [9], and it was possible to register pre-acquired CT to PET using a standard registration algorithm, such as the mutual information method [10]. Another issue is the influence of the headrest used to stabilize the patient's head. Brain CT images include the headrest of the CT system; therefore, the accuracy of PET attenuation correction may be degraded by using the  $\mu$ -map which includes a different headrest for PET systems. If the headrest of the CT system is larger than that of the PET system, the uptake on the backside of the brain is overestimated. Consequently, the image uniformity and quantitative accuracy may be degraded. The effects of different headrests on PET images should be known when using pre-acquired CT images for PET AC; however, this has not yet been investigated. Furthermore, it is unclear whether it

is necessary to replace different CT headrests with the same headrest in a PET system.

In this study, we evaluated the effects of  $\mu$ -maps generated from CT images including a different headrest on PET images. In addition, we proposed an automated method for removing headrests from CT images using a combination of simple image-processing algorithms. For clinical validation, the  $\mu$ -maps with the headrest removed by the automated method (proposed method) were compared with those with the headrest removed manually by a radiological technologist (reference standard) in standardized uptake values of the reconstructed PET images using each  $\mu$ -map.

## 2 Materials and methods

Figure 1 shows the headrest of the Discovery MI PET/CT (GE Healthcare, Milwaukee, WI, USA) and VRAIN used in this study. The CT acquisition parameters for Discovery MI were as follows: 120 kV, 200 mA; voxel size,  $0.5469 \times 0.5469$  mm; slice thickness, 3.75 mm, and matrix size,  $512 \times 512$  pixels. As shown in Fig. 2, the headrest of Discovery MI wraps around the head from the bottom, left, and right sides, which is similar in shape to the headrest of general CT systems; however, the headrest of VRAIN supports only the lower part of the head.

### 2.1 An automated CT headrest removal method

We preliminarily examined brain CT images acquired using several scanners and found the following characteristics: a cushion was used to isolate the head region from the headrest. The patient's head was fixed using a band from the front of the face to both ends of the headrest.

Considering the above characteristics, we proposed an algorithm to automatically remove the headrest from brain CT images. The process flow is shown in Fig. 3. First, we determined the threshold value using Otsu's method [11] and then obtained the mask using a binarization process (a). An opening process was used to remove the band region in front of the forehead (b). In the next step, segmentation was used to identify the air inside the head and fill it with mask values (c). The headrest region was then removed by another opening process (d), and the remaining isolated regions were removed by segmentation (e). The final head mask was applied to the original CT image.

We preliminarily tested the proposed automated method using 481 human-head CT images available on a website (<http://headctstudy.qure.ai/#paper>) [12]. The dataset included data from GE BrightSpeed, GE Discovery CT750 HD, GE LightSpeed, GE Optima CT660, Philips MX 16-slice, and Philips Access-32 CT scanners (six scanners in total). Pixel sizes ranged from 0.21 to 0.98 mm. The headrest

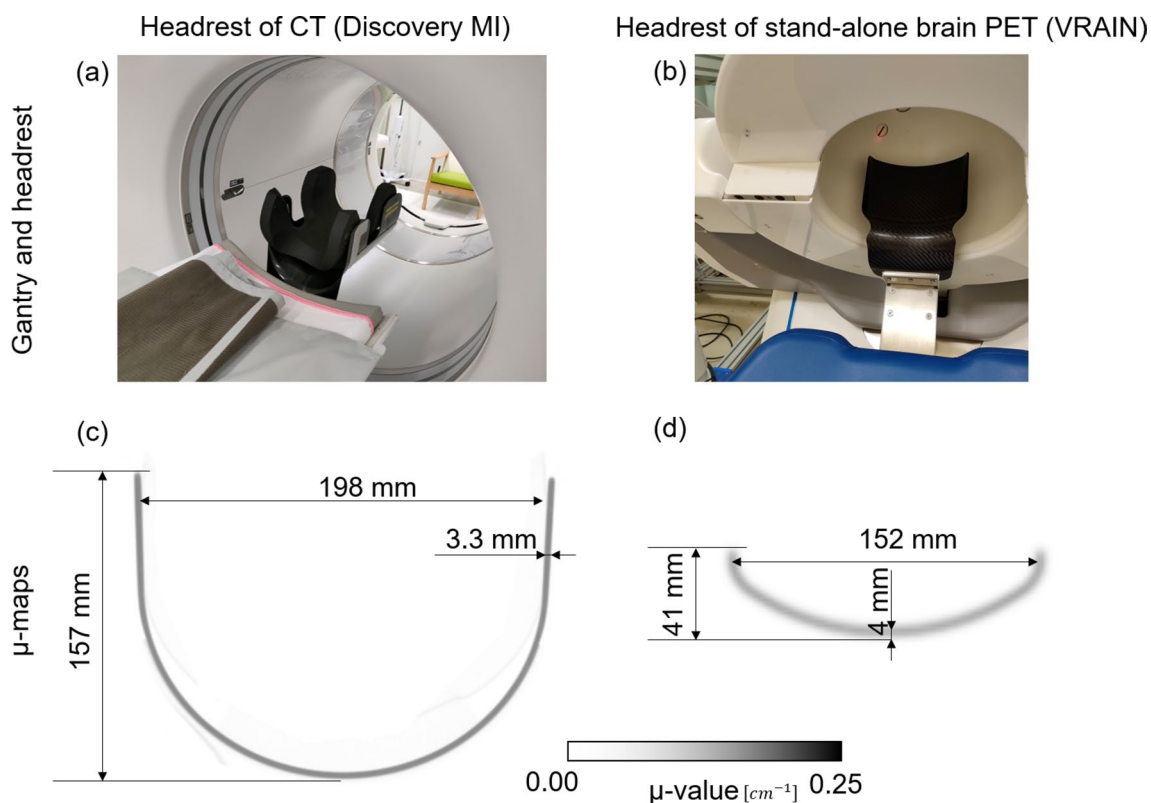


**Fig. 2** Photographs (upper) and  $\mu$ -maps (lower) of headrests of Discovery MI (a) and VRAIN (b)

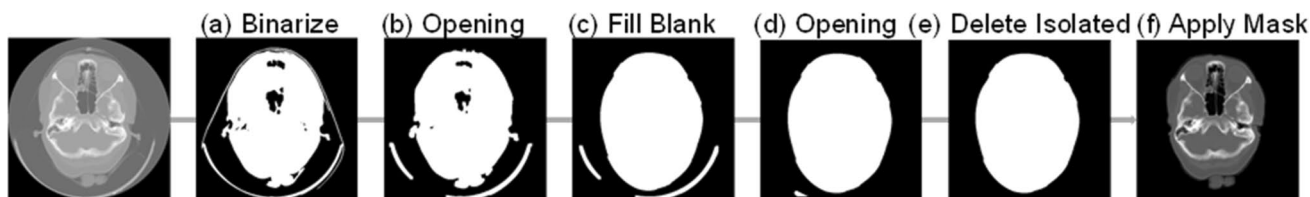


**Fig. 3** Proposed image-processing workflow for removing a headrest from CT images

of all data was successfully removed using the automated method, except for one (Supplementary Fig. 1). The reason for this failure was the tuft of wet hair that was directly in contact with the headrest. While visual inspection is needed, we believe that the automated headrest removal method is applicable not only to Discovery MI but also to a wide variety of CT systems.

## 2.2 Phantom evaluation of the effects of headrests

A cylindrical phantom with an inner diameter of 155 mm was uniformly filled with an  $^{18}\text{F}$  solution of 10 MBq at the beginning of the measurement and measured for 30 min in the list mode with VRAIN using the headrest of VRAIN. Image reconstruction was performed using the

ordered-subsets expectation–maximization (OSEM) method, including scatter correction using a single scattering simulation method based on the  $\mu$ -map [13]. The voxel size was  $2.0 \times 2.0 \times 2.0 \text{ mm}^3$ , the matrix size was  $140 \times 140 \times 112$  pixels, and the post-smoothing filter was a 3-D Gaussian filter with a 4 mm full width at half maximum (FWHM).

To create three different types of  $\mu$ -maps, first we performed a CT scan of the cylindrical phantom with the headrest attached to Discovery MI. A  $\mu$ -map based on this CT image had a different headrest from VRAIN's, so we called it  $\mu$ -map-*diffHr* in this paper. Next, the headrest region in the CT images was removed by a radiological technologist to make a  $\mu$ -map without the headrest ( $\mu$ -map-*noHr*). Finally, we took CT images of the headrest of VRAIN, and replaced

the headrest region of the  $\mu$ -map-*diffHr* with the  $\mu$  values of the headrest of *VRAIN* ( $\mu$ -map-*sameHr*).

The PET images using the three different  $\mu$ -maps were evaluated by the following metrics including quantitative bias, uniformity, and noise [14, 15]. A large circular ROI (nROI) with a diameter of 130 mm was placed on the central slice of the phantom. The quantitative bias was measured using the following equation:

$$\text{Quantitative bias} = \frac{nROI_{mean} - \text{true activity concentration}}{\text{true activity concentration}} \times 100\% \tag{1}$$

where  $nROI_{mean}$  is the mean value within the nROI and  $\text{true activity concentration}$  is the true activity per unit volume (kBq/mL).

For the uniformity evaluation, 17 circular ROIs (uROIs) of 500 mm<sup>2</sup> were placed on the central slice of the phantom and two other slices  $\pm 40$  mm away from the central slice (51 uROIs in total). Uniformity was calculated using the following equation:

$$\text{Uniformity} = \sqrt{\frac{1}{n} \sum_{i=1}^n \left( \frac{uROI_{mean}}{uROI_{TOT}} - 1 \right)^2} \tag{2}$$

where  $uROI_{mean}$  is the mean value within each ROI and  $uROI_{TOT}$  is the mean value of all ROIs ( $n = 51$ ). Noise was calculated using the nROI and the following equation:

$$\text{Noise} = \frac{SD_{nROI}}{nROI_{mean}} \times 100\% \tag{3}$$

where  $SD_{nROI}$  is the standard deviation of nROI. Acceptance criteria were  $\pm 10\%$  for the quantitative bias, 0.0249 for the uniformity, and 15% for the noise [14, 16–18].

### 2.3 Clinical evaluation of the effects of headrests

To validate the  $\mu$ -map created by the automated method of removing the headrest (automated  $\mu$ -map-*noHr*), we performed a human study. We obtained sets of individual brain PET, CT, and magnetic resonance imaging (MRI) images from 10 healthy male volunteers (aged 22–47 years). None of the participants had a history of brain injury, psychiatric

disease, or any abnormal MRI findings. <sup>18</sup>F-FDG ( $288 \pm 27$  MBq) was administered after a fast of at least 6 h. Forty-five minutes after administration, the forehead and chin were fixed with bands, and a 10-min PET scan was performed with *VRAIN*. This study was conducted in accordance with the Declaration of Helsinki and approved by the Institutional Review Board of our hospital. Informed consent was obtained from all the participants. This study was registered with the Japan Registry of Clinical Trials (jRCTs032210086).

Image reconstruction parameters were the same as those described in “An automated CT headrest removal method”. PET images were reconstructed with automated  $\mu$ -map-*noHr*, with manual  $\mu$ -map-*noHr* where the headrest was manually removed by a radiological technologist (G.A.), and with  $\mu$ -map-*sameHr* which was made by combining the  $\mu$ -map of the headrest of *VRAIN* with the manual  $\mu$ -map-*noHr*.

The mean standard uptake values (SUVs) in nine major regions, including the frontal, mesial temporal, lateral temporal, parietal and occipital lobes, posterior cingulate cortex, precuneus, striatum, and cerebellum, were compared between the two PET images. We used PMOD ver. 3.7 (PMOD Technologies, Zürich, Switzerland) for the volume of interest (VOI) analysis. The PET images were co-registered with individual 3-D T1-weighted MRI images. MRI was used for spatial normalization (anatomical standardization). The automatic-anatomical-labeling (AAL) VOI template was applied to individual PET images using the inverse transformation parameters of the MRI-based spatial normalization.

The mean SUVs of the nine brain regions were compared using the Wilcoxon signed-rank test. A  $p$ -value of less than 0.05 was considered to be statistically significant.

## 3 Results

### 3.1 Phantom evaluation

The respective values of the quantitative bias, uniformity, and noise are listed in Table 1. All values were within the criteria except for the uniformity of images with

**Table 1** Quantitative bias, uniformity, and noise for PET images reconstructed with three different types of  $\mu$ -maps

	$\mu$ -map- <i>diffHr</i>	$\mu$ -map- <i>noHr</i>	$\mu$ -map- <i>sameHr</i>	Criteria
Quantitative bias (%)	8.1	0.36	2.1	$\leq \pm 10$
Uniformity	0.0293	0.0165	0.0162	$\leq 0.0249$
Noise (%)	5.84	5.55	5.46	$\leq 15$

$\mu$ -map-*diffHr*,  $\mu$ -map based on a pre-acquired CT where the headrest is different from PET  
 $\mu$ -map-*noHr*,  $\mu$ -map where the different headrest was removed  
 $\mu$ -map-*sameHr*,  $\mu$ -map with the same headrest as PET



$\mu$ -map-*diff*Hr. The uniformity and noise of images with  $\mu$ -map-*no*Hr were slightly ( $\sim 2\%$ ) degraded compared with those with  $\mu$ -map-*same*Hr. The quantitative bias with  $\mu$ -map-*no*Hr was 1.7% lower than that with  $\mu$ -map-*same*Hr. The reconstructed images of a cylindrical phantom using the three different types of  $\mu$ -maps are shown in Fig. 4, where those using  $\mu$ -map-*diff*Hr had higher values than the others.

### 3.2 Clinical evaluation

The representative images of manual  $\mu$ -map-*no*Hr, automated  $\mu$ -map-*no*Hr,  $\mu$ -map-*same*Hr, and human FDG-PET images using each  $\mu$ -map are shown in Fig. 5. The automated method completely removed the headrest without any deficiencies in the head regions, and the PET images were visually identical to those of the other conditions. No significant differences were found in the mean SUVs of the

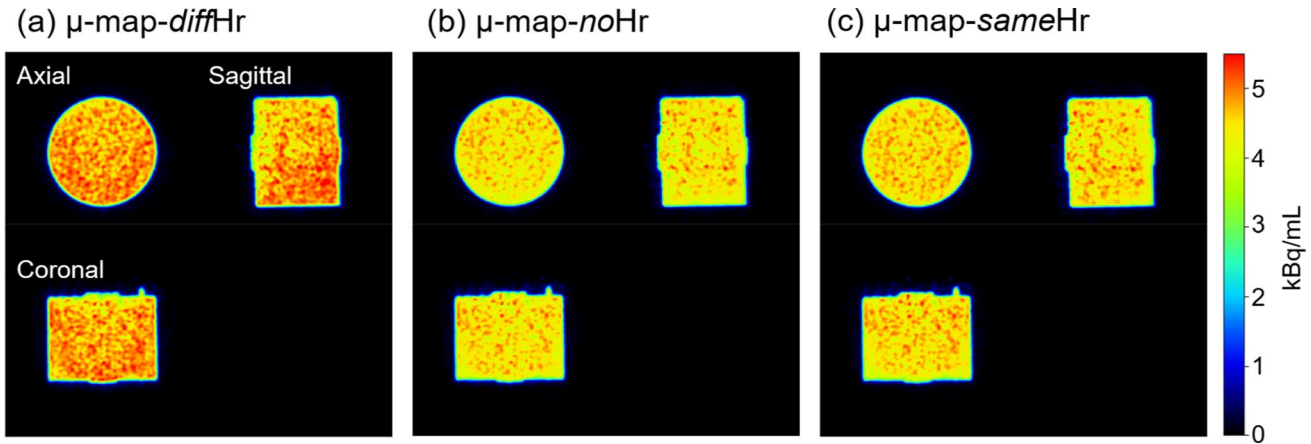


**Fig. 4** Reconstructed images of a cylindrical phantom using three different types of  $\mu$ -maps: (a)  $\mu$ -map-*diff*Hr,  $\mu$ -map based on a pre-acquired CT where the headrest is different from PET; (b)  $\mu$ -map-

*no*Hr,  $\mu$ -map where the different headrest was removed; (c)  $\mu$ -map-*same*Hr,  $\mu$ -map with the same headrest as PET

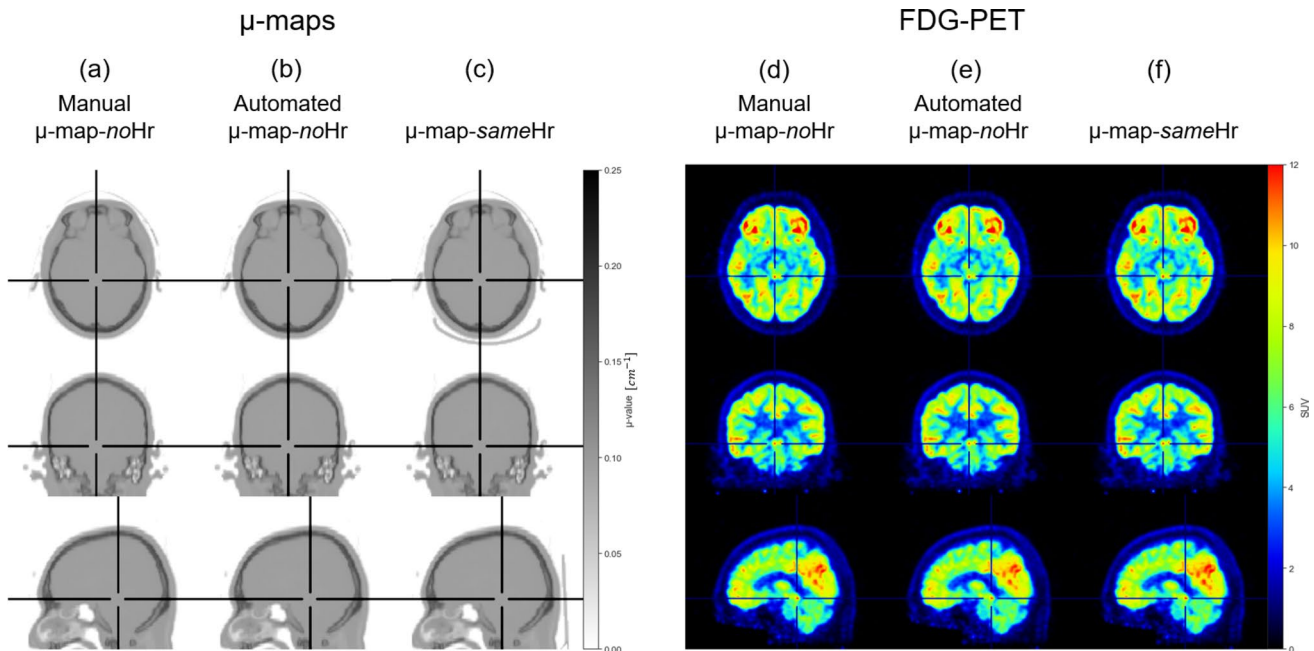


**Fig. 5** Representative three different types of  $\mu$ -maps: manual  $\mu$ -map-*no*Hr (a), automated  $\mu$ -map-*no*Hr (b), and  $\mu$ -map-*same*Hr (c), FDG-PET images reconstructed using the manual  $\mu$ -map-*no*Hr (d), the automated  $\mu$ -map-*no*Hr (e), and the  $\mu$ -map-*same*Hr (f)

nine VOIs between the PET images reconstructed with the three  $\mu$ -maps (Fig. 6).

## 4 Discussion

In this study, we evaluated the effect of different  $\mu$ -maps on PET images, such as a  $\mu$ -map with a CT headrest which was different from the PET's headrest, and a  $\mu$ -map where the headrest was removed from the CT images. As a result, removing the different headrests from the  $\mu$ -maps was effective; therefore, we developed an automated method of removing headrests from CT images and validated it using human brain FDG-PET data.

Using a  $\mu$ -map including a different headrest, the uniformity of the PET image did not reach the criteria and showed higher voxel values entirely. AC basically was performed to recover the PET voxel values which degraded by headrest; therefore, the  $\mu$ -map including the larger CT headrest caused the overcorrection of the PET voxel values.

The uniformity (0.0293) also deviated from the criteria (uniformity:  $\leq 0.0249$ ) [15]. Furthermore, there were no artifacts on PET images reconstructed using the  $\mu$ -maps in which the headrest was removed (Fig. 4). Although the uniformity and noise of the phantom PET image with  $\mu$ -map-*noHr* were slightly ( $< 2\%$ ) degraded compared to those with  $\mu$ -map-*sameHr*, they were satisfied with the acceptance criteria. The quantitative bias was 2.1% in  $\mu$ -map-*sameHr* and 0.36% in  $\mu$ -map-*noHr*. Although the quantitative bias in  $\mu$ -map-*noHr* was closer to the true value, it does not indicate that  $\mu$ -map-*noHr* provides better quantitative accuracy. We believe the quantitative bias in  $\mu$ -map-*noHr* accidentally approached 0% by various mixed positive and negative biases. This is supported by the results that uniformity and noise were the best for the  $\mu$ -map-*sameHr* condition.

These results suggest that we should remove the different headrest from the  $\mu$ -map for AC. The effect of the headrest of VRAIN was small enough ( $< 2\%$  difference), using the  $\mu$ -map without the headrest would be acceptable for brain PET AC. Another option is to artificially add the headrest of

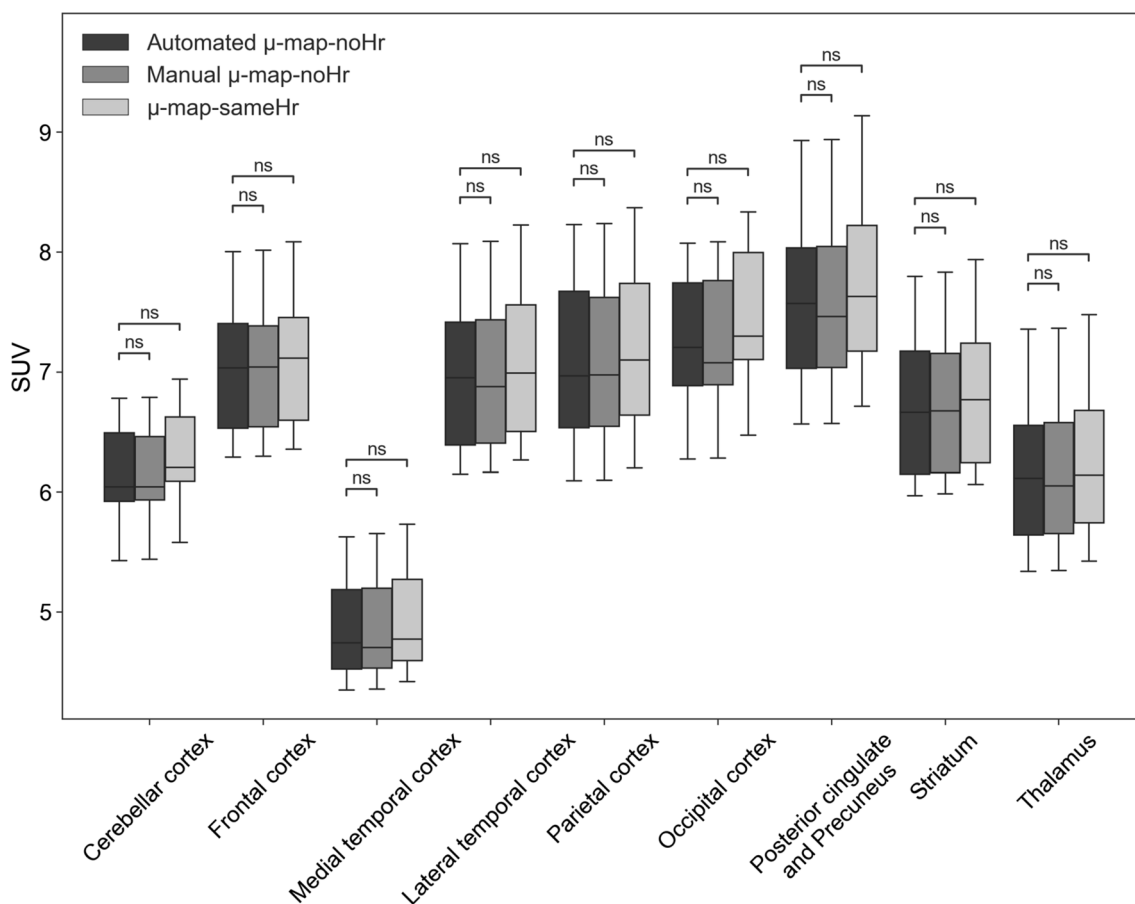


**Fig. 6** Box-and-whisker plots of SUVs of nine brain regions. There was no statistical difference in SUVs between PET images with the different  $\mu$ -maps: manual  $\mu$ -map-*noHr*, headrest was manually removed from CT images; automated  $\mu$ -map-*noHr*, headrest was

automatically removed;  $\mu$ -map-*sameHr*, the headrest of VRAIN was inserted in the manual  $\mu$ -map-*noHr*. Central horizontal line, median value; horizontal ends of the box, upper and lower quartiles; the bar ends, maximum and minimum values

the VRAIN; however, the position of the headrest cannot be determined from the PET images. To avoid the mispositioning error, we decided to use the  $\mu$ -map without the headrest. We propose an automated method that combines simple image-processing methods, and believe that this method is applicable to clinical images.

There are some other options for preparing a  $\mu$ -map for stand-alone PET. The first estimates the attenuation coefficients from MRI [19]. Although additional CT scans can be avoided, the estimation accuracy has only been evaluated in adult brains with normal anatomy [20]. Theoretically speaking, the CT-based approach outperforms the MRI-based estimation in terms of the  $\mu$ -map accuracy. Another option is to use deep learning-based methods based on PET images alone [21, 22]. However, the accuracy of this method was insufficient. Lee et al. reported that deep learning-based methods tend to underestimate brain PET intensity in the frontal and occipital lobes [23]. In addition, some AC methods using time-of-flight (TOF) information have been proposed [24, 25]; however, the current timing resolution of PET systems is not sufficient to generate the accurate  $\mu$ -map. To improve the accuracy of these methods, it is essential to improve the timing performance [26]. The required timing resolution depends on the noise levels of the coincidence count data and the complexity of the attenuation coefficient distributions (i.e., imaging targets) [27]. Further investigation is needed to reduce the effect of noise even with a 10 ps timing resolution [28]. We believe that our proposed method using pre-acquired CT images can theoretically provide more accurate  $\mu$ -maps compared to such MRI-, TOF-, and deep learning-based methods.

One limitation of this pre-acquired CT-based AC approach is the scan coverage of head CT images. For an accurate AC, CT images should cover the top of the head to the bottom of the cerebellum. If a part of the head is lacking in CT images, further processing, such as image completion, is required for accurate AC.

## 5 Conclusion

We evaluated the influence of different headrests on the  $\mu$ -map for PET AC. Our results showed that the  $\mu$ -map including different headrests caused artifacts on PET images, but the  $\mu$ -map after removing the headrest was acceptable. Therefore, we developed an automated method to remove headrests from CT images. In human studies, the proposed automated method of headrest removal provided equivalent  $\mu$ -maps and PET images compared with the manual method. Pre-acquired CT-based AC with automated headrest removal is useful for stand-alone brain PET systems such as VRAIN to ensure the quantitative accuracy of PET images without additional radiation exposure to patients.

**Supplementary Information** The online version contains supplementary material available at <https://doi.org/10.1007/s12194-023-00744-z>.

## Declarations

**Conflict of interest** This clinical study was financially supported by ATOX Co., Ltd. (Tokyo, Japan).

**Ethics approval** All the procedures performed in studies involving human participants were in accordance with the ethical standards of the institutional and/or national research committee and with the 1964 Helsinki Declaration and its later amendments or comparable ethical standards. This study was approved by the institutional review board of our institute and registered in the Japan Registry of Clinical Trials (jRCTs032210086).

## References

1. Bailey DL. Transmission scanning in emission tomography. *Eur J Nucl Med.* 1998;25(7):774–87. <https://doi.org/10.1007/S002590050282>.
2. Kinahan PE, Hasegawa BH, Beyer T. X-ray-based attenuation correction for positron emission tomography/computed tomography scanners. *Semin Nucl Med.* 2003;33(3):166–79. <https://doi.org/10.1053/SNUC.2003.127307>.
3. Tashima H, Yamaya T. Proposed helmet PET geometries with add-on detectors for high sensitivity brain imaging. *Phys Med Biol.* 2016;61(19):7205–20. <https://doi.org/10.1088/0031-9155/61/19/7205>.
4. Watanabe M, et al. Performance evaluation of a high-resolution brain PET scanner using four-layer MPPC DOI detectors. *Phys Med Biol.* 2017;62(17):7148–66. <https://doi.org/10.1088/1361-6560/AA82E8>.
5. Yoshida E, et al. 245 ps-TOF brain-dedicated PET prototype with a hemispherical detector arrangement. *Phys Med Biol.* 2020. <https://doi.org/10.1088/1361-6560/AB8C91>.
6. Akamatsu G, et al. Performance evaluation of VRAIN: a brain-dedicated PET with a hemispherical detector arrangement. *Phys Med Biol.* 2022. <https://doi.org/10.1088/1361-6560/ac9e87>.
7. Takahashi M, Akamatsu G, Iwao Y, Tashima H, Yoshida E, Yamaya T. Small nuclei identification with a hemispherical brain PET. *EJNMMI Phys.* 2022;9(1):1–11. <https://doi.org/10.1186/S40658-022-00498-4/TABLES/2>.
8. Chen W. Clinical applications of PET in brain tumors. *J Nucl Med.* 2007;48(9):1468–81. <https://doi.org/10.2967/JNUMED.106.037689>.
9. Marinelli M, Positano V, Tucci F, Neglia D, Landini L. Automatic PET-CT image registration method based on mutual information and genetic algorithms. *Sci World J.* 2012;2012:12. <https://doi.org/10.1100/2012/567067>.
10. Maes F, Collignon A, Vandermeulen D, Marchal G, Suetens P. Multimodality image registration by maximization of mutual information. *IEEE Trans Med Imaging.* 1997;16(2):187–98. <https://doi.org/10.1109/42.563664>.
11. Tashima H, Akamatsu G, Yamashita T, Yamaya T. Scatter correction with image-domain interpolation for TOF helmet-type PET. *IEEE NSS/MIC conference record 2021*; 1–2.
12. Verwer EE, et al. Harmonisation of PET/CT contrast recovery performance for brain studies. doi: <https://doi.org/10.1007/s00259-021-05201-w/Published>.
13. Ikari Y, et al. Phantom criteria for qualification of brain FDG and amyloid PET across different cameras. *EJNMMI Phys.*

- 2016;3(1):1–18. <https://doi.org/10.1186/S40658-016-0159-Y/TABLES/4>.
14. Sankur B. Survey over image thresholding techniques and quantitative performance evaluation. *J Electron Imaging*. 2004;13(1):146. <https://doi.org/10.1117/1.1631315>.
  15. Vandenberghe S, Marsden PK. PET-MRI: a review of challenges and solutions in the development of integrated multimodality imaging. *Phys Med Biol*. 2015;60(4):R115. <https://doi.org/10.1088/0031-9155/60/4/R115>.
  16. Sunderland JJ, Christian PE. Quantitative PET/CT scanner performance characterization based upon the Society of Nuclear Medicine and Molecular Imaging Clinical Trials Network oncology clinical simulator phantom. *J Nucl Med*. 2023;56:145–52.
  17. Scheuermann JS, Saffer JR, Karp JS, Levering AM, Siegel BA. Qualification of PET scanners for use in multicenter cancer clinical trials: the American College of Radiology Imaging Network experience. *J Nucl Med*. 2023;50:1187–93.
  18. PET Amyloid Biomarker Committee. <sup>18</sup>F-labeled PET tracers targeting amyloid as an imaging biomarker. Quantitative imaging biomarkers alliance. technically confirmed version. Jun 3, 2022. Available from; RSNA.ORG/QIBA
  19. Ladefoged CN, et al. A multi-centre evaluation of eleven clinically feasible brain PET/MRI attenuation correction techniques using a large cohort of patients. *Neuroimage*. 2017;147:346–59. <https://doi.org/10.1016/J.NEUROIMAGE.2016.12.010>.
  20. Liu F, Jang H, Kijowski R, Zhao G, Bradshaw T, McMillan AB. A deep learning approach for <sup>18</sup>F-FDG PET attenuation correction. *EJNMMI Phys*. 2018;5(1):1–15. <https://doi.org/10.1186/S40658-018-0225-8>.
  21. Dong X, et al. Synthetic CT generation from non-attenuation corrected PET images for whole-body PET imaging. *Phys Med Biol*. 2019. <https://doi.org/10.1088/1361-6560/AB4EB7>.
  22. Lee JS. A review of deep-learning-based approaches for attenuation correction in positron emission tomography. *IEEE Trans Radiat Plasma Med Sci*. 2021;5(2):160–84. <https://doi.org/10.1109/TRPMS.2020.3009269>.
  23. Rezaei A, Defrise M, Nuyts J. ML-reconstruction for TOF-PET with simultaneous estimation of the attenuation factors. *IEEE Trans Med Imaging*. 2014;33(7):1563–72. <https://doi.org/10.1109/TMI.2014.2318175>.
  24. Chun SY, Kim KY, Lee JS, Fessler JA. Joint estimation of activity distribution and attenuation map for TOF-PET using alternating direction method of multiplier. Proceedings - International Symposium on Biomedical Imaging, 2016;pp. 86–89. doi: <https://doi.org/10.1109/ISBI.2016.7493217>.
  25. Chilamkurthy S, et al. Development and validation of deep learning algorithms for detection of critical findings in head CT scans. 2018; Accessed: 13 Jun 2022. [Online]. Available: <http://arxiv.org/abs/1803.05854>
  26. Boellaard R, Hofman MBM, Hoekstra OS, Lammertsma AA. Accurate PET/MR quantification using time-of-flight MLAA image reconstruction. *Mol Imag Biol*. 2014;16:469–77.
  27. Rezaei A, et al. Simultaneous reconstruction of activity and attenuation in time-of-flight PET. *IEEE Trans Med Imag*. 2023;31:2224–33.
  28. Lecoq P, et al. Roadmap toward the 10 ps time-of-flight PET challenge. *Phys Med Biol*. 2023;65:2101.

**Publisher's Note** Springer Nature remains neutral with regard to jurisdictional claims in published maps and institutional affiliations.

Springer Nature or its licensor (e.g. a society or other partner) holds exclusive rights to this article under a publishing agreement with the author(s) or other rightsholder(s); author self-archiving of the accepted manuscript version of this article is solely governed by the terms of such publishing agreement and applicable law.